A Geostrophic Adjustment Model of Two Buoyant Fluids

CLAUDIA CENEDESE

Department of Physical Oceanography, Woods Hole Oceanographic Institution, Woods Hole, Massachusetts

JAMES A. LERCZAK

College of Earth, Ocean, and Atmospheric Sciences, Oregon State University, Corvallis, Oregon

GIUSEPPE BARTONE

Department of Civil, Building, and Environmental Engineering, Sapienza University of Rome, Rome, Italy

(Manuscript received 16 September 2011, in final form 6 April 2012)

ABSTRACT

A combination of analytical calculations and laboratory experiments has been used to investigate the geostrophic adjustment of two buoyant fluids having different densities in a third denser ambient fluid. The frontal position, the depth profile, and the horizontal and vertical alignments of the two buoyant fluids at the final equilibrium state are determined by the ratio of the baroclinic Rossby radii of deformation $\Gamma_1 = \lambda_{31}/\lambda_{21}$ and $\Gamma_2 = \lambda_{32}/\lambda_{21}$ and the Burger numbers $B_1 = \lambda_{31}/L_1$ and $B_2 = \lambda_{32}/L_2$ of the two buoyant fluids, where $\lambda_{ij} = (\sqrt{g'_{ij}H_j}/f)$ is the baroclinic Rossby radius of deformation between fluids i and j. The buoyant fluids 1 and 2 have densities ρ_1 and ρ_2 ($\rho_1 < \rho_2$), respectively; the ambient denser fluid has density ρ_3; g' is the reduced gravity; H and L are the buoyant fluids' initial depth and width, respectively; and f is the Coriolis parameter. Laboratory rotating experiments confirmed the analytical prediction of the location of the two fronts. After reaching geostrophic equilibrium, the two buoyant currents align mainly horizontally when the extent of the fronts between fluids 1 and 3 and between fluids 2 and 3 is large compared to the extent of the front between fluids 1 and 2: that is, large values of λ_{31} and λ_{32} compared to λ_{21} or equivalently $\Gamma_1 \gg 1$ and $\Gamma_2 \gg 1$. Alternatively, if the extent of the fronts between the three fluids is similar (i.e., $\Gamma_1 \approx \Gamma_2 \approx 1$), the buoyant currents align mainly vertically. Furthermore, the Burger number of the lightest fluid B_1 controls the distance of the inner front from the coast, while B_2 controls the offshore extent of the outer front.

1. Introduction

Buoyant coastal currents are often composed of several plumes emanating from spatially separated rivers. Examples include the Western Maine Coastal Current (WMCC), which receives its buoyant waters principally from the Kennebec and Penobscot Rivers (Franks and Anderson 1992; Geyer et al. 2004; Churchill et al. 2005); the western Adriatic coastal current, which is driven by the Po River and a series of smaller rivers draining the Apennine mountains in eastern Italy (Raicich 1996; Artegiani et al. 1997); and the Alaska Coastal Current, which receives its freshwater from many small streams draining the Alaskan coastal mountain ranges (Royer 1982, 1998; Stabeno et al. 2004).

The dynamics of buoyant coastal currents have been studied extensively in the past (e.g., O'Donnell 1990; Yankovsky and Chapman 1997; Garvine 2001; Fong and Geyer 2002; Garcia Berdeal et al. 2002; Hetland 2005). In particular, laboratory experiments have brought numerous insights on the scales adopted by these flows and their dynamics and stability (Griffiths and Linden 1981a; Lentz and Helfrich 2002). However, the study of how two or more buoyant currents interact and how the water masses of individual currents align relative to each other vertically and horizontally has received little scientific attention. Yet, the problem of multiplume interactions is a scientifically interesting problem with societal and ecological significance (e.g., relating to the fate of pollutants, harmful algal blooms, larval dispersal, and population connectivity).

Corresponding author address: Claudia Cenedese, Woods Hole Oceanographic Institution, 360 Woods Hole Rd., Woods Hole, MA 02536.
E-mail: ccenedese@whoi.edu

DOI: 10.1175/JPO-D-11-0169.1

Buoyancy-driven currents occur when a fluid is released into an ambient fluid of different density: for example, a river flowing into the open ocean. If the fluid is lighter, it will flow above the ambient fluid as what we will herein refer to as a buoyant current. The outer edges of these currents are bounded by fronts. In the presence of rotation, the horizontal spreading of these buoyancy-driven currents is restrained by the Coriolis force. In the presence of vertical walls (i.e., a coastline), the condition of no flow normal to the wall implies that there is no Coriolis force parallel to the wall. Motion can occur parallel to the wall accompanied by a Coriolis force directed normal to the wall. Hence, the resulting current hugs the wall with the wall on its right looking downstream (in the Northern Hemisphere). We will refer to these currents as buoyant coastal currents.

A buoyant coastal current can flow along a sloping wall in one of two forms: (i) a surface-trapped current or (ii) a slope-controlled current. A surface-trapped current forms a shallow layer that intersects the bottom slope close to the free surface intersection of the current with the slope, herein called shore, and bottom topography has virtually no effect on its dynamics. Numerous studies have examined the behavior (formation, propagation, stability, etc.) of a surface-trapped current along a vertical wall (over a flat bottom) in various configurations (e.g., Griffiths and Hopfinger 1983; Griffiths and Linden 1981a, 1982; Chabert d'Hieres et al. 1991; Garvine 1999; Fong and Geyer 2002; Geyer et al. 2004). A slope-controlled current is fundamentally different, because bottom topography plays a leading dynamical role (Chapman and Lentz 1994; Yankovsky and Chapman 1997; Lentz and Helfrich 2002). In this study, we will limit our investigation to surface-trapped currents.

The goal of this study is to use a combination of analytical calculations and laboratory experiments to investigate the relative vertical and horizontal alignment of two buoyant fluids of different densities after they reach a geostrophic equilibrium. The analytical calculations show how different horizontal and vertical alignment scenarios are obtained by varying the densities and volume transports of the two buoyant coastal currents. These different scenarios are presented as a function of the dynamically relevant nondimensional numbers. Laboratory rotating experiments confirm the analytical prediction of the depth profile and location of the two buoyant currents.

The paper is organized as follows: The geostrophic adjustment model is discussed in section 2. The model results are illustrated in section 3. The laboratory experimental apparatus and measurement techniques are described in section 4. A typical experiment is described in section 5 together with the frontal position measurements and the comparison with the model prediction. The conclusions of this work are discussed in section 6.

2. The model

An idealized, linearized model has been developed to investigate the relative vertical and horizontal alignments of two surface-trapped buoyant coastal currents after they reach geostrophic equilibrium. Geostrophic adjustment models (Rossby 1938; Gill 1982) have been used by various investigators to study the structure of steady flows in the vicinity of fluids with contrasting densities (Csanady 1971; Hsueh and Cushman-Roisin 1983). For example, Csanady (1979) and Griffiths and Linden (1981b) describe the geostrophic adjustment of an axisymmetric vortex in an ambient fluid of contrasting density and infinite depth, while Griffiths and Linden (1982) describe the geostrophic adjustment of an idealized density-driven boundary current. Ou (1983) applied a geostrophic adjustment model to describe the frontal structure and velocity distribution of an idealized shelf-slope front. Ou (1984) studied the geostrophic adjustment of a two-dimensional fluid initially at rest, but with a continuous lateral density gradient in order to demonstrate a mechanism for frontogenesis. As a final example, van Heijst (1985) considered the geostrophic adjustment of three fluids with contrasting density to study the structure of the density field and circulation in the vicinity of an idealized tidal mixing front. To the authors' knowledge, the van Heijst (1985) model is the only other application of a geostrophic adjustment model to three fluids. However, it considers a very different geometry and initial conditions from the model presented in this study. Our application of a three-fluid geostrophic adjustment model to two adjacent coastal currents is unique, it provides a base state for a complete stability analysis, and it is an interesting geophysical problem that sheds some insight on how buoyant coastal currents interact in the environment. Given the large number of dimensional and nondimensional parameters contained in the model (see below), the horizontal and vertical alignment of the two buoyant currents as these parameters vary is nonintuitive.

The model considered here consists of three homogeneous, incompressible, and immiscible fluids denoted by 1, 2, and 3 of densities $\rho_1 < \rho_2 < \rho_3$, respectively, whose initial state is as shown in Fig. 1a. A solid vertical wall representing the coastline is indicated by the thick solid line. Two vertical barriers (dashed lines) separate the three fluids. The system is rotating with angular velocity $f/2$, where f is the Coriolis parameter. A Cartesian coordinate system (x, y, z) is introduced with x and y directed parallel and orthogonal to the vertical wall, respectively, and z directed upward from the free surface. We assume there are no variations in the direction along the wall (x direction). The vertical wall position is $y = 0$ and the two barriers are located at $y = L_1$ and

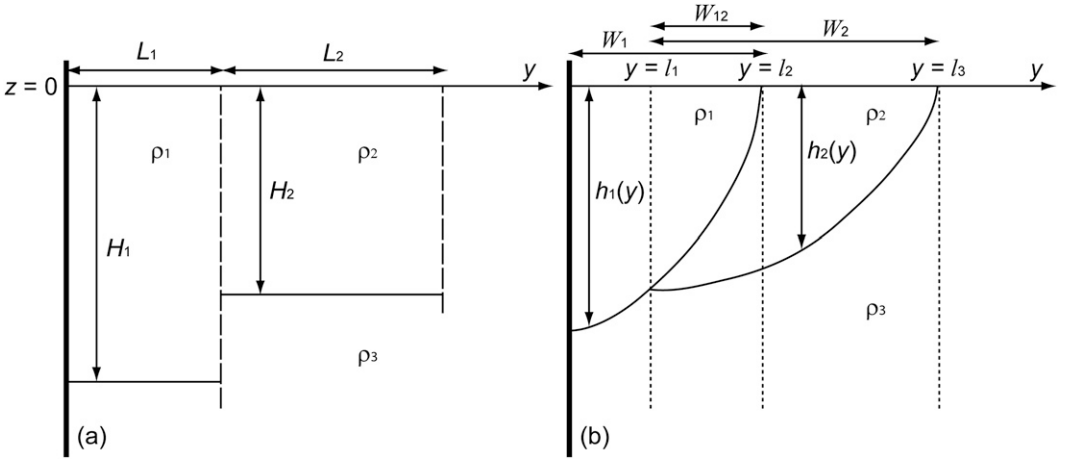

FIG. 1. Geometry of the model for the geostrophic adjustment of two buoyant fluids. (a) Sketch of the initial state ($t = 0$) with the two barriers (dashed lines) separating three fluids. (b) Sketch of the adjusted equilibrium state ($t = t_{eq}$) in which the two buoyant currents are in geostrophic balance. Dotted lines indicate the position of the two surface fronts ($y = l_2$ and $y = l_3$) and one subsurface front ($y = l_1$). Not to scale.

$y = L_1 + L_2$. The initial depth of fluid 1 (fluid 2) is H_1 (H_2), while the ambient fluid 3 is considered to be infinitely deep and at rest.

When the barriers are removed, fluid 1 (fluid 2) tends to intrude into fluid 2 (fluid 3) until a state of equilibrium is reached. Assuming that the adjustment process is inviscid and in the absence of mixing, potential vorticity in each individual fluid layer will be conserved. In the final, adjusted state, the resulting flow is assumed to be in geostrophic balance and directed along the wall, as indicated by the final adjusted state of the interfaces between the fluids schematically shown in Fig. 1b.

With the above assumptions, it is possible to derive a set of coupled hyperbolic equations with general solutions for the equilibrium depths of fluids 1 and 2, $h_1(y)$ and $h_2(y)$, respectively, as well as for the cross-shore structure of the along-wall velocity u_i in each of the buoyant currents in the regions $0 \le y \le l_1$, $l_1 < y < l_2$, and $l_2 \le y \le l_3$, where l_1 is the position of fluid 2 subsurface front and $l_2(l_3)$ the position of the fluid 1 (fluid 2) surface front (Fig. 1b). We will focus on cases in which $l_1 \ge 0$ and $l_3 \ge l_2$.

Conservation of potential vorticity in fluids 1 and 2 requires

$$\frac{f - \dfrac{\partial u_1}{\partial y}}{h_1} = \frac{f}{H_1} \quad \text{and} \tag{1a}$$

$$\frac{f - \dfrac{\partial u_2}{\partial y}}{h_2} = \frac{f}{H_2}. \tag{1b}$$

In the adjusted state, the along-wall flow in each fluid is in geostrophic balance, giving

$$u_1 = -\frac{g'_{31}}{f}\frac{\partial h_1}{\partial y} \quad \text{for} \quad 0 \le y \le l_1, \tag{2a}$$

$$u_1 = -\frac{1}{f}\left(g'_{31}\frac{\partial h_1}{\partial y} + g'_{32}\frac{\partial h_2}{\partial y}\right) \quad \text{for} \quad l_1 < y < l_2, \tag{2b}$$

$$u_2 = -\frac{1}{f}\left(g'_{32}\frac{\partial h_1}{\partial y} + g'_{32}\frac{\partial h_2}{\partial y}\right) \quad \text{for} \quad l_1 < y < l_2, \quad \text{and} \tag{2c}$$

$$u_2 = -\frac{g'_{32}}{f}\frac{\partial h_2}{\partial y} \quad \text{for} \quad l_2 \le y \le l_3, \tag{2d}$$

where $g'_{ij} = g[(\rho_i - \rho_j)/\rho_0]$ is the reduced gravity between fluids i and j, and ρ_0 is a reference density. Equations (2a)–(2d) are derived under the assumption that the density differences are small enough in order to take the ratios ρ_1/ρ_2, ρ_1/ρ_3, and $\rho_2/\rho_3 \approx 1$.

In the adjusted state, the region $0 \le y \le l_1$ is characterized by a two-layer stratification of densities ρ_1 and ρ_3. An equation for the upper-layer depth h_1 can be obtained by combination of (1a)–(2a), yielding

$$\frac{\partial^2 h_1}{\partial y^2} - \frac{1}{\lambda_{31}^2}h_1 = -\frac{H_1}{\lambda_{31}^2}, \tag{3}$$

where $\lambda_{ij} = \sqrt{g'_{ij}H_j}/f$ is the baroclinic Rossby radius of deformation between fluids i and j. The general solution is

$$h_1 = Ee^{y/\lambda_{31}} + Fe^{-y/\lambda_{31}} + H_1, \tag{4}$$

where E and F are unknown constants of integration.

A three-layer stratification is present in the region $l_1 < y < l_2$. As before, using Eqs. (1a), (1b), (2b), and (2c) one can derive the equations for the upper- (h_1; i.e., fluid 1) and middle- (h_2; i.e., fluid 2) layer depths,

$$\frac{\partial^4 h_1}{\partial y^4} - \left(\frac{\lambda_{32}^2 + \lambda_{31}^2}{\lambda_{21}^2\lambda_{32}^2}\right)\frac{\partial^2 h_1}{\partial y^2} + \frac{1}{\lambda_{21}^2\lambda_{32}^2}h_1 = +\frac{H_1}{\lambda_{21}^2\lambda_{32}^2} \quad \text{and} \tag{5a}$$

$$h_2 = \frac{H_2}{H_1}\left(-\lambda_{21}^2\frac{\partial^2 h_1}{\partial y^2} + h_1 - H_1\frac{\rho_2 - \rho_1}{\rho_1}\right). \tag{5b}$$

The general solutions are

$$h_1 = Ae^{\sqrt{\alpha_1}y} + Be^{-\sqrt{\alpha_1}y} + Ce^{\sqrt{\alpha_2}y} + De^{-\sqrt{\alpha_2}y} + H_1 \quad \text{and} \tag{6a}$$

$$h_2 = \frac{H_2}{H_1}[(Ae^{\sqrt{\alpha_1}y} + Be^{-\sqrt{\alpha_1}y})(1 - \alpha_1\lambda_{21}^2) + (Ce^{\sqrt{\alpha_2}y} + De^{-\sqrt{\alpha_2}y})(1 - \alpha_2\lambda_{21}^2) + H_1], \tag{6b}$$

respectively, where A, B, C, and D are unknown constants of integration and

$$\alpha_1 = \frac{1}{2}\left(\frac{\lambda_{32}^2 + \lambda_{31}^2}{\lambda_{21}^2\lambda_{32}^2} - \sqrt{\frac{\lambda_{32}^4 - \lambda_{31}^4 + 2\lambda_{32}^2\lambda_{31}^2 - 4\lambda_{21}^2\lambda_{32}^2}{\lambda_{21}^2\lambda_{32}^2}}\right) \tag{7a}$$

and

$$\alpha_2 = \frac{1}{2}\left(\frac{\lambda_{32}^2 + \lambda_{31}^2}{\lambda_{21}^2\lambda_{32}^2} + \sqrt{\frac{\lambda_{32}^4 - \lambda_{31}^4 + 2\lambda_{32}^2\lambda_{31}^2 - 4\lambda_{21}^2\lambda_{32}^2}{\lambda_{21}^2\lambda_{32}^2}}\right). \tag{7b}$$

For the two-layer region $l_2 \le y \le l_3$, an equation for h_2 can be derived in a similar way, yielding

$$\frac{\partial^2 h_2}{\partial y^2} - \frac{1}{\lambda_{32}^2}h_2 = -\frac{H_2}{\lambda_{32}^2}, \tag{8}$$

with general solution

$$h_2 = Ge^{y/\lambda_{32}} + Ke^{-y/\lambda_{32}} + H_2, \tag{9}$$

where G and K are unknown constants of integration.

The various unknown constants of integration A–G and K are determined by matching the solutions across the boundaries $y = l_1$ and $y = l_2$ and by applying conditions following from mass conservation and geometry. Because the unknowns l_1, l_2, and l_3 also appear in the boundary conditions, 11 conditions are required in order to determine all the unknowns in the problem. These boundary conditions are as follows:

1) The velocity at the wall (i.e., $y = 0$) is equal to a constant u_0 ($u_0 = 0$ in the absence of background flow).
2) The layer thickness h_1 is continuous across $y = l_1$.
3) The velocity u_1 is continuous across $y = l_1$.
4) The layer thickness h_1 vanishes at the surface front $y = l_2$.
5) The layer thickness h_2 vanishes at the surface front $y = l_3$.
6) The layer thickness h_2 vanishes at the subsurface front $y = l_1$.
7) The layer thickness h_2 is continuous across $y = l_2$.
8) The velocity u_2 is continuous across $y = l_2$.
9) The velocity u_2 at $y = l_1$ can be obtained by integrating the x-momentum equation $\partial u_2/\partial t - f v = 0$ in time from $t = 0$ to $t = t_{eq}$, where t_{eq} is the time at which the final adjusted equilibrium state is reached and for which the boundary conditions are sought. Knowing that at $t = 0$ the velocity $u_2 = 0$, the velocity u_2 at $t = t_{eq}$ is $u_2 = f[y(t = t_{eq}) - y(t = 0)]$. Since we are interested in the velocity u_2 at $y = l_1$, we have that $y(t = t_{eq}) = l_1$ and $y(t = 0) = L_1$; hence, $u_2 = f(l_1 - L_1)$.
10) Conservation of mass of fluid 1 requires $H_1L_1 = \int_0^{l_2} h_1(y)\,dy$.
11) Conservation of mass of fluid 2 requires $H_2L_2 = \int_{l_1}^{l_3} h_2(y)\,dy$.

These conditions yield a set of equations of varying complexity in the unknowns A–G, K, l_1, l_2, and l_3, for which, due to nonlinearity, no analytical solutions could be obtained. Hence, the system was solved using a standard numerical Matlab routine.

3. Model results

Solutions to the equations obtained in section 2 have been calculated for different values of the fluids' baroclinic Rossby radii of deformation and Burger numbers. The depth profile of the two buoyant fluids are shown in Fig. 2, where two different scenarios are plotted. As suggested by the equations in section 2, the different vertical and horizontal alignments of the two buoyant fluids, after they reach the geostrophic equilibrium, depend on the two ratios of the three baroclinic Rossby radii of deformation, $\Gamma_1 = \lambda_{31}/\lambda_{21}$ and $\Gamma_2 = \lambda_{32}/\lambda_{21}$. The baroclinic Rossby radius represents a length scale of the width of the front between the different fluids. For simplicity, we define the width of the front between fluids 1 (2) and 3 as $W_1 = l_2$ ($W_2 = l_3 - l_1$) and the width of the front between fluids 1 and 2 (i.e., the extent over which the two buoyant currents overlap) as $W_{12} = l_2 - l_1$ (Fig. 1b). Note that W_1 (W_2) is not an accurate measure

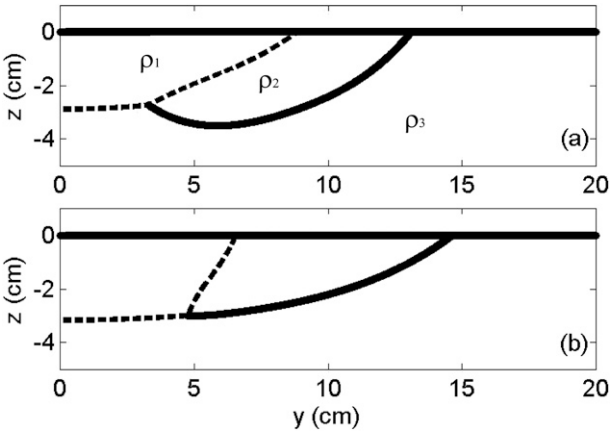

FIG. 2. Depth profile of two buoyant coastal currents after the geostrophic adjustment takes place. The dashed (solid) line indicates the model prediction of the depth $h_1(y)$ [$h_2(y)$]. The coastal vertical wall is located at $y = 0$ cm. Both fluid 1 and fluid 2 flow out of the page. Values are (a) $\Gamma_1 = 1.3, \Gamma_2 = 0.8, B_1 = 0.9$, and $B_2 = 0.6$ and (b) $\Gamma_1 = 4.5, \Gamma_2 = 4.5, B_1 = 0.9$, and $B_2 = 0.9$. Note that laboratory parameters have been used in the model calculations. Hence, the dimensions are in centimeters on the axes.

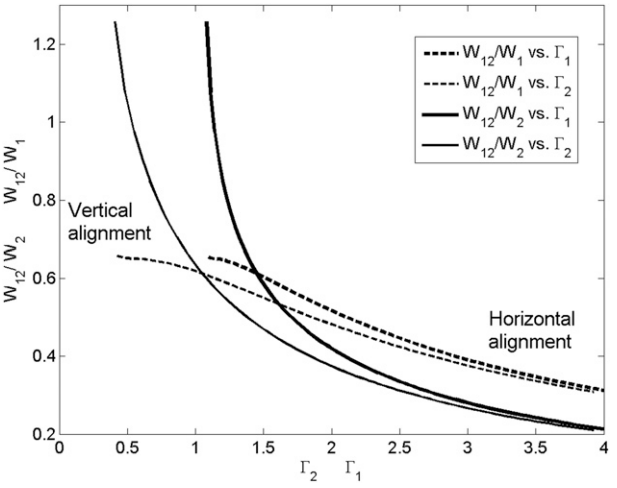

FIG. 3. Dependence of parameters W_{12}/W_1 and W_{12}/W_2 on Γ_1 and Γ_2 for $B_1 = B_2 = 1.0$ and $H_1 = H_2 = 2.5$ cm. For $\Gamma_1 \approx \Gamma_2 \approx 1$ the two buoyant coastal currents will mainly overlap [i.e., $W_{12}/W_1 \sim W_{12}/W_2 \sim O(1)$] and present a vertical alignment. For $\Gamma_1 \gg 1$ and $\Gamma_2 \gg 1$, the two buoyant coastal currents have little vertical overlap relative to the width of the buoyant currents (i.e., $W_{12}/W_1 \ll 1$ and $W_{12}/W_2 \ll 1$) and present a horizontal alignment. The parameter space shown in this figure is obtained by keeping the densities ρ_1 and ρ_3 constant and equal to 0.9987 and 1.0222, respectively, and by varying the density ρ_2.

of the width of the front between fluids 1 (2) and 3 for cases with a significant overlap between fluids 1 and 2.

When $W_1 \gg W_{12}$ and $W_2 \gg W_{12}$ (i.e., large values of λ_{31} and λ_{32} compared to λ_{21} or equivalently $\Gamma_1 \gg 1$ and $\Gamma_2 \gg 1$), one expects the two buoyant fluids to have little vertical overlap, relative to the width of the buoyant currents, and present a horizontal alignment (Fig. 2b). Alternatively, if the width of the fronts between the three fluids is similar (i.e., $\Gamma_1 \approx \Gamma_2 \approx 1$), one expects that the two buoyant currents will mainly overlap and present a vertical alignment (Fig. 2a). Hence, with increasing values of Γ_1 and Γ_2 and fixed values of the Burger numbers, the alignment of the two buoyant coastal currents will shift from a scenario in which the two currents are mainly vertically aligned [i.e., $W_{12}/W_1 \approx O(1)$ and $W_{12}/W_2 \approx O(1)$] to a scenario in which the alignment is mainly horizontal (i.e., $W_{12}/W_1 \ll 1$ and $W_{12}/W_2 \ll 1$; Fig. 3).

The dependence of the parameters W_{12}/W_1 and W_{12}/W_2 on Γ_1 and Γ_2 shown in Fig. 3 was obtained by keeping the densities ρ_1 and ρ_3 constant and equal to 0.9987 and 1.0222, respectively, and by varying the density ρ_2 in order to change the magnitude of Γ_1 and Γ_2. This approach is identical to the one used in the laboratory experiments (Table 1). Furthermore, the value of $H_1 = H_2 = 2.5$ cm and the Burger numbers $B_1 = \lambda_{31}/L_1$ and $B_2 = \lambda_{32}/L_2$ were constant and equal to 1.0. The values of L_1 and L_2 were dictated by the values of the Burger numbers and the Rossby radii of deformations. It is important to notice that Γ_1 and Γ_2 are not independent parameters: an increase in Γ_1 determines an increase in Γ_2, as also shown in Table 1. The choice of keeping $H_1 = H_2 = 2.5$ cm, keeping ρ_1 and ρ_3 fixed, and varying ρ_2 is a specific choice we made (others are possible) in order to investigate the parameter space in Fig. 3. Figure 3 shows that for $\Gamma_1 \approx \Gamma_2 \approx 1$ the value of W_{12}/W_2 is a few times larger than W_{12}/W_1. The $O(1)$ values of Γ_i are obtained by a large value of ρ_2. Consequently, the small value of λ_{32} requires a small value of L_2 in order to have a constant B_2. Small values of L_2 limit the extent of the outer front (i.e., W_2) and cause the large values of W_{12}/W_2 shown in Fig. 3.

The Burger numbers of the two buoyant fluids control the position of the two buoyant coastal current fronts relative to the coastal wall. In particular, the Burger number of the lightest fluid B_1 controls the distance of the inner front from the coastal wall, as shown in Fig. 4. By ''inner'' front, we refer to the front between fluids 1 and 2 and between fluids 1 and 3 (dashed line in Fig. 2). By ''outer'' front, we refer to the front between fluids 2 and 3 (solid line in Fig. 2). For increasing values of B_1 and constant values of Γ_1 and Γ_2, the inner front moves toward the coastal wall, as indicated by the change in location of $y = l_1$ (solid line in Fig. 5a). A change in B_1, while keeping constant the other nondimensional parameters, leaves the values of W_{12} and W_2 unaltered (Figs. 4a–c, 5a). The width and therefore the offshore extent of the outer front is controlled by B_2. For increasing values of B_2, while keeping constant the other nondimensional parameters,

TABLE 1. Values of the parameters used in the experiments. Units are in centimeter–gram–second (CGS) system. From the definition in section 2, $L_1 = R_1$ and $L_2 = R_2 - R_1$. The Coriolis parameter is fixed at $f = 2\ s^{-1}$ and the maximum depth of the densest water in the tank is kept constant at $H = 25$ cm.

Expt No.	ρ_1	ρ_2	ρ_3	$H_1 = H_2$	L_1	L_2	Γ_1	Γ_2	B_1	B_2
1	0.9987	1.0150	1.0222	3.5	8	8	1.2	0.7	0.56	0.31
2	0.9987	1.0150	1.0222	2.5	12	4	1.2	0.7	0.32	0.52
3	0.9987	1.0150	1.0222	2.5	6	10	1.2	0.7	0.63	0.21
4	0.9987	1.0100	1.0222	2.5	8	8	1.4	1.0	0.47	0.34
5	0.9987	1.0100	1.0222	2.5	12	4	1.4	1.0	0.32	0.68
6	0.9987	1.0100	1.0222	2.5	6	10	1.4	1.0	0.63	0.27
7	0.9987	1.0050	1.0222	2.0	8	8	1.9	1.6	0.42	0.36
8	0.9987	1.0050	1.0222	2.5	12	4	1.9	1.6	0.32	0.81
9	0.9987	1.0050	1.0222	2.0	6	10	1.9	1.6	0.57	0.29

the outer front moves toward the coastline (thick lines in Fig. 5b). A change in B_2 influences neither W_{12} nor the location of $y = l_1$; hence, the position of the inner front remains almost unchanged (Figs. 4d–f, 5b).

The two extreme scenarios illustrated in Fig. 2 present Burger numbers $O(1)$. The alignment of the two buoyant coastal currents for the same values of Γ_1 and Γ_2 are slightly modified when considering Burger numbers that are not $O(1)$ (Fig. 6). In particular, if $\Gamma_1 \approx \Gamma_2 \approx 1$ and B_1 and B_2 are $O(1)$, the alignment between the two buoyant coastal currents is vertical (Fig. 6a), but for $B_1 \ll 1$ and $B_2 \ll 1$ (Fig. 6b) the alignment becomes horizontal in that the width of the front between fluids 1 and 2 W_{12} is now small compared to W_1 and W_2 because of the large

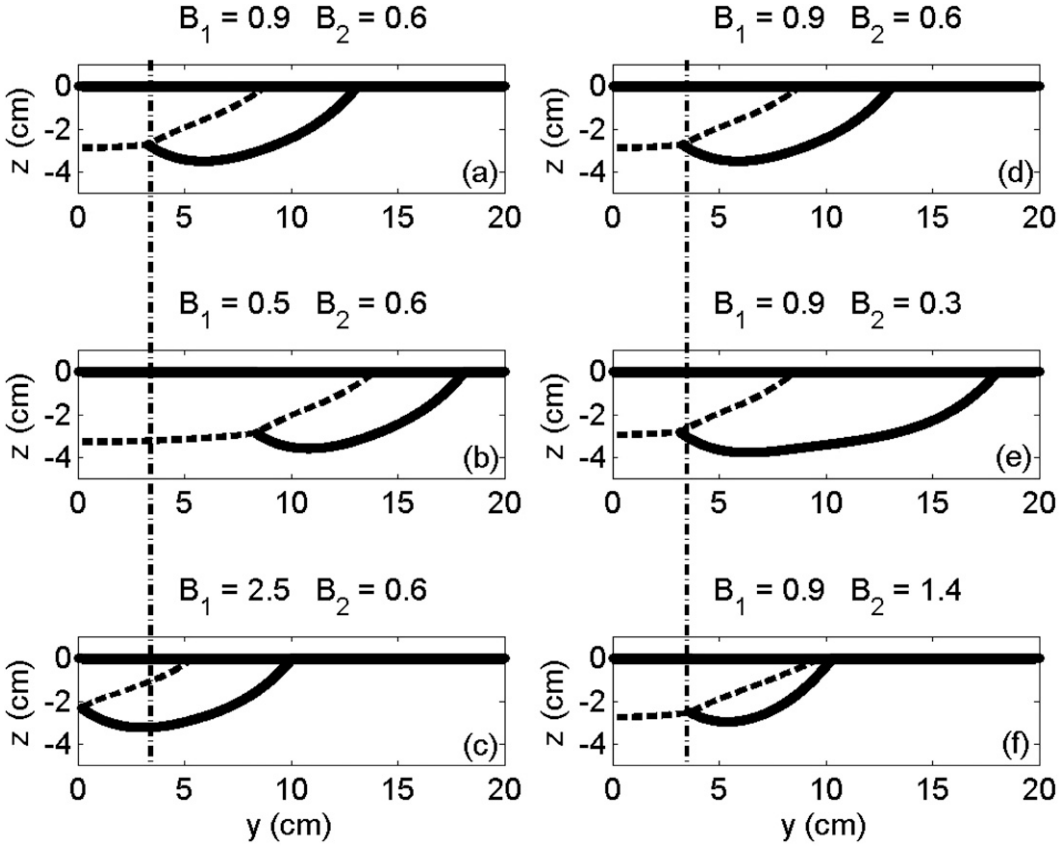

FIG. 4. Depth profile of two buoyant coastal currents for different values of Burger numbers and fixed values of $\Gamma_1 = 1.3$ and $\Gamma_2 = 0.8$. The lines in the figure have the same meaning as in Fig. 2. The dashed–dotted line indicates the position of $y = l_1$ for $B_1 = 0.9$ and $B_2 = 0.6$. Values are (a) $B_1 = 0.9$ and $B_2 = 0.6$; (b) $B_1 = 0.5$ and $B_2 = 0.6$; (c) $B_1 = 2.5$ and $B_2 = 0.6$; (d) $B_1 = 0.9$ and $B_2 = 0.6$; (e) $B_1 = 0.9$ and $B_2 = 0.3$; and (f) $B_1 = 0.9$ and $B_2 = 1.4$.

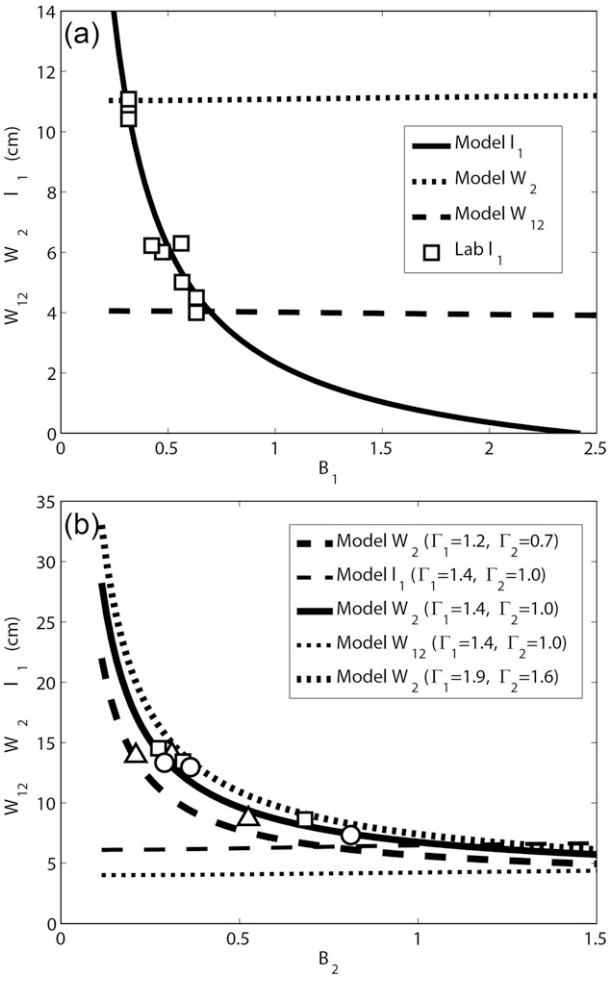

FIG. 5. Dependence of parameters W_{12}, l_1, and W_2 on the Burger numbers (a) $B_1 = \lambda_{31}/L_1$ and (b) $B_2 = \lambda_{32}/L_2$. In (a), for increasing values of B_1 the inner front (solid line) moves toward the coastal wall (i.e., l_1 decreases). A change in B_1 leaves the values of W_{12} (dashed line) and W_2 (dotted line) unaltered. Squares represent the value of l_1 for the laboratory experiments. The other nondimensional parameters assume the following values: $\Gamma_1 = 1.4$, $\Gamma_2 = 1.0$, $B_2 = 0.4$, and $H_1 = H_2 = 2.5$ cm. In (b), for increasing values of B_2 the outer front moves toward the coastline (i.e., W_2 decreases). Symbols represent the value of W_2 for the laboratory experiments. The dependence of W_2 on B_2 is shown for three different values of Γ_i: $\Gamma_1 = 1.2$ and $\Gamma_2 = 0.7$ (thick dashed line and triangles), $\Gamma_1 = 1.4$ and $\Gamma_2 = 1.0$ (thick solid line and squares), and $\Gamma_1 = 1.9$ and $\Gamma_2 = 1.6$ (thick dotted line and circles). A change in B_2 influences neither W_{12} nor l_1. In (b), $B_1 = 0.5$ and $H_1 = H_2 = 2.5$ cm. The parameter spaces shown in this figure are obtained by keeping the densities ρ_1 and ρ_3 constant and equal to 0.9987 and 1.0222, respectively, and by varying the density ρ_2.

amount of fluids 1 and 2 present. For the case in which $\Gamma_1 \gg 1$, $\Gamma_2 \gg 1$, and B_1 and B_2 are $O(1)$, the alignment is horizontal (Fig. 6c), but for $B_1 \gg 1$, and $B_2 \gg 1$ (Fig. 6d) the alignment becomes vertical given the lack of fluids 1 and 2. Both the inner and outer fronts move closer to the vertical wall and W_{12} is now comparable to W_1 and W_2.

In summary, the model of the geostrophic adjustment of two buoyant fluids having different densities in a third denser ambient fluid suggest that, after reaching a geostrophic equilibrium, for Burger numbers $O(1)$ the two buoyant currents align mainly horizontally for $\Gamma_1 \gg 1$ and $\Gamma_2 \gg 1$ with very little vertical overlap. In the case in which $\Gamma_1 \approx \Gamma_2 \approx 1$, the buoyant currents align mainly vertically. Variation in the Burger number of the two buoyant fluids will modify the position of the two buoyant fronts relative to the coastal wall. Finally, intermediate scenarios between the two extremes presented above can occur. For example, for $\Gamma_1 \gg 1$ and $\Gamma_2 \approx 1$, horizontal alignment between the two currents persists, but with a significant overlap region (not shown).

4. Experimental apparatus

The experiments are conducted in a Plexiglas square tank of depth 35 cm and length and width 60 cm. The tank is mounted on a 1-m-diameter anticlockwise rotating turntable with a vertical axis of rotation (Fig. 7). We use a square tank to avoid optical distortion from side views associated with a circular tank. The tank is filled to a height H with salted dense water of density ρ_3, which is initially in solid-body rotation. Two concentric bottomless cylinders are centered on the axis of rotation and immersed to the required depth in the ambient fluid of density ρ_3 to generate the barriers between the three fluids. The cylinders are withdrawn vertically while the table is rotating via a pulley system. Care is taken to minimize any mixing between the three fluids. Two dyed fluids of density $\rho_1 < \rho_2$ ($<\rho_3$) are added inside the concentric cylinders until they form layers of depth H_1 and H_2, respectively. Fluid of density ρ_1 is added in the inner cylinder of radius R_1, while fluid of density ρ_2 is added in the outer cylinder of radius R_2 (Fig. 7). The whole system is left to reach a state of solid-body rotation before the experiment begins with the vertical withdrawal of the bottomless cylinders. The density difference between the three fluids is produced by the addition of different amounts of salt to the fluids.

The method described above to generate buoyant currents is referred to as "constant volume" since the amount of buoyant fluid in the cylinders is fixed. A different method to generate a buoyant current is the so-called constant flux in which buoyant fluid is released at a fixed rate by a source positioned near a vertical (or sloping) wall. Griffiths and Linden (1981b) discuss in detail the similarities and differences between these two different methods of generating buoyant currents. Our choice of constant volume experiments is mainly dictated by the simplicity of the setup and the similarity of the initial conditions to the analytical model presented in section 2.

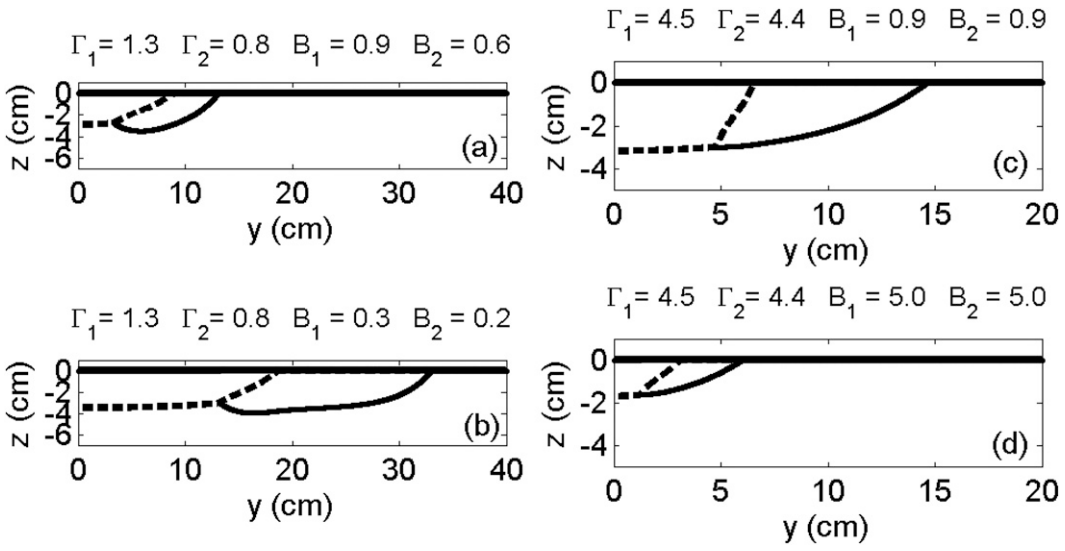

FIG. 6. Depth profile of two buoyant coastal currents for different values of Burger numbers. (a),(c) As in Figs. 2a, b, respectively. Values are (a) $\Gamma_1 = 1.3, \Gamma_2 = 0.8, B_1 = 0.9$, and $B_2 = 0.6$; (b) $\Gamma_1 = 1.3, \Gamma_2 = 0.8, B_1 = 0.3$, and $B_2 = 0.2$; (c) $\Gamma_1 = 4.5, \Gamma_2 = 4.5, B_1 = 0.9$, and $B_2 = 0.9$; and (d) $\Gamma_1 = 4.5, \Gamma_2 = 4.5, B_1 = 5.0$, and $B_2 = 5.0$. Note the different axes' size between (a) and (b) and between (c) and (d), necessary to clearly visualize both (b) and (d).

Furthermore, the circular geometry is chosen to remove unwanted "end" effects. With this method, we avoid issues related to the "nose" of the currents (i.e., the furthermost along-wall location of the buoyant current where along-wall horizontal gradients of density are very large and where the buoyant currents "begin"; see Simpson 1997) and the formation of a "bulge" near the source (e.g., Garvine 2001; Nof 2005; Horner-Devine et al. 2006), which occur when the constant flux method is used.

A camera positioned on one side of the tank acquires a side view of the currents. To measure the depth profile of the two buoyant currents, we dye the two fluids with water-soluble fluorescent dyes: Sodic Fluorescein for the fluid with density ρ_1, and Rhodamine B for the fluid with density ρ_2. The vertical plane passing through the center of the cylinders is illuminated with a 5-W light-emitting diode (LED) having two different wavelengths, a cyan light (emission peak at 505 nm) for the Fluorescein excitation, and a green light (530 nm) for the excitation of Rhodamine B. A 20-cm fiber-optic light guide, ending with a rectangular light line, is used in order to minimize the light lost and reduction of intensity with distance. The illuminating system produces a divergent light beam; hence, a convex cylindrical lens is located between the tank and the light source in order to focus the light into a thin sheet (width of about 0.3 cm) lying

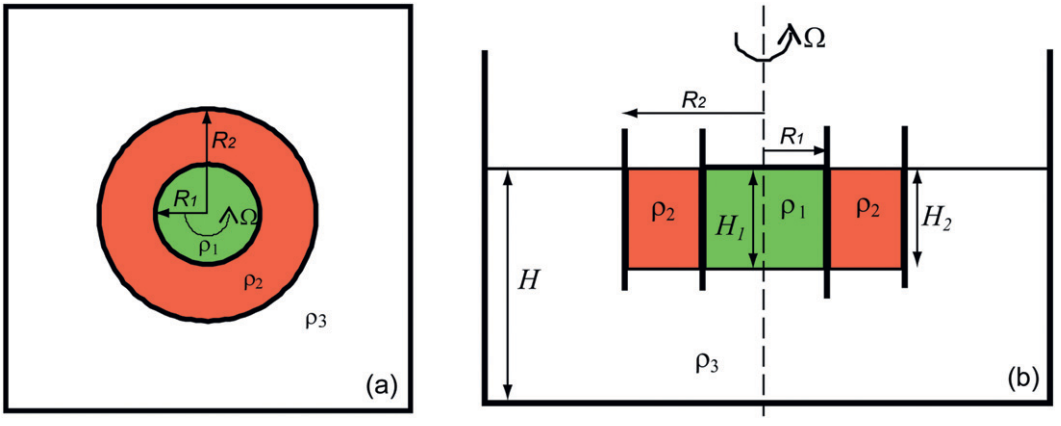

FIG. 7. Sketch of the experimental apparatus: (a) top view and (b) side view. The dashed line in (b) indicates the axis of rotation, and $\Omega = f/2\ \mathrm{s}^{-1}$ is the angular velocity of the rotating table. Not to scale.

on the plane orthogonal to the flow direction and passing through the center of the cylinders. Images of the depth profile are calibrated and compared to the model prediction (section 2).

A total of nine experiments are presented. The maximum depth of the densest water in the tank is kept constant at $H = 25$ cm, as well as the value of the Coriolis parameter $f = 2\ \mathrm{s}^{-1}$. The initial depths of the buoyant fluids are the same (i.e., $H_1 = H_2$) and ranged from 2.0 to 3.5 cm. The value of the densities and the cylinders' radii are varied in order to obtain different values of Γ_i and B_i for $i = 1, 2$. In particular, the densities ρ_1 and ρ_3 are kept constant and equal to 0.9987 and 1.0222, respectively, and the density ρ_2 is varied (Table 1). The buoyancy forces are controlled by the reduced gravity g'_{ij} between fluids i and j, which assumed values $g'_{31} = 22.8\,\mathrm{cm\,s^{-2}}$, $6.9 \le g'_{32} \le 16.6\,\mathrm{cm\,s^{-2}}$, and $6.1 \le g'_{21} \le 15.8\,\mathrm{cm\,s^{-2}}$. Finally, the cylinders radii varied between $6 \le R_1 \le 12$ cm while $R_2 = 16$ cm was kept constant. The values of the above parameters for each experiment are shown in Table 1 together with the values of the relevant nondimensional parameters in the ranges $1.2 \le \Gamma_1 \le 1.9$, $0.7 \le \Gamma_2 \le 1.6$, $0.3 \le B_1 \le 0.6$, and $0.2 \le B_2 \le 0.8$.

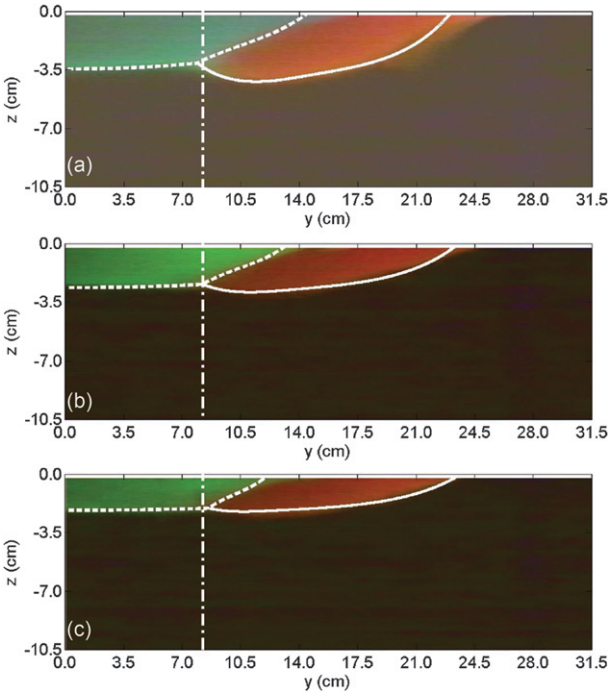

FIG. 8. Side view of the two buoyant currents after reaching the geostrophic equilibrium. Values are (a) $\Gamma_1 = 1.2, \Gamma_2 = 0.7, B_1 = 0.56$, and $B_2 = 0.31$; (b) $\Gamma_1 = 1.4, \Gamma_2 = 1.0, B_1 = 0.47$, and $B_2 = 0.34$; and (c) $\Gamma_1 = 1.9, \Gamma_2 = 1.6, B_1 = 0.42$, and $B_2 = 0.36$. The dashed (solid) line indicates the model prediction of the depth $h_1(y)$ [$h_2(y)$]. The dashed–dotted line indicates the position of $y = l_1$ in (b).

5. The geostrophic adjustment

During each experiment, after the vertical withdrawal of the bottomless cylinders, the two buoyant fluids evolved until they reached geostrophic equilibrium. Initially both fluids spread horizontally radially outward from the axis of rotation. In the presence of rotation, the horizontal spreading of these buoyant fluids is restrained by the Coriolis force. A radial motion induces an azimuthal flow to conserve angular momentum, and this flow, in turn, produces a radial Coriolis force that opposes the buoyancy force (i.e., geostrophic balance). Consequently, further radial motion is inhibited and closed streamlines develop (i.e., vortices). A geostrophic balance is reached within a few inertial periods.

The axisymmetric geometry used in the laboratory is equivalent to the geometry shown in Fig. 1a in which a vertical wall is present. In the laboratory, the vertical wall is represented by the vertical line passing through the center of the tank (Griffiths and Linden 1981a,b). Furthermore, the laboratory geometry assumes periodic boundary conditions in the x direction (i.e., a fluid element moves along closed streamlines). The two buoyant currents are represented in the laboratory by two concentric vortices. In this study, we are interested in the final horizontal and vertical alignment of the two buoyant fluids, not in their downstream evolution, which cannot be captured by these experiments. Hence, the model represents one-half of a vertical section of the vortices formed in the laboratory, in which the coastline is the center of the vortex. We do not expect the presence of a vertical wall to modify the results presented below.

Once the two concentric vortices are in geostrophic balance over a flat bottom, wavelike disturbances appear at the inner and outer fronts and they ultimately grow to large amplitude (Cenedese and Linden 2002; Griffiths and Linden 1981a,b). The laboratory results suggest that the solutions found in section 2 should be unstable to a combination of baroclinic/barotropic instability (Griffiths and Linden 1981a,b) after a transient state, which lasts a few inertial periods. The present study focuses solely on the geostrophic adjustment of the two buoyant fluids and a future contribution will discuss in detail the stability of the two buoyant currents' fronts.

After the two buoyant fluids reach the final adjusted equilibrium state the buoyant currents present a depth profile as shown in Figs. 8 and 9. The model prediction of the depths $h_1(y)$ (dashed line) and $h_2(y)$ (solid line) are superimposed on the images acquired during the laboratory experiments. To compare the model prediction and the image from the laboratory experiments a calibration of the image was conducted to convert pixels into distance (cm). In the laboratory image the location $y = l_1$ was

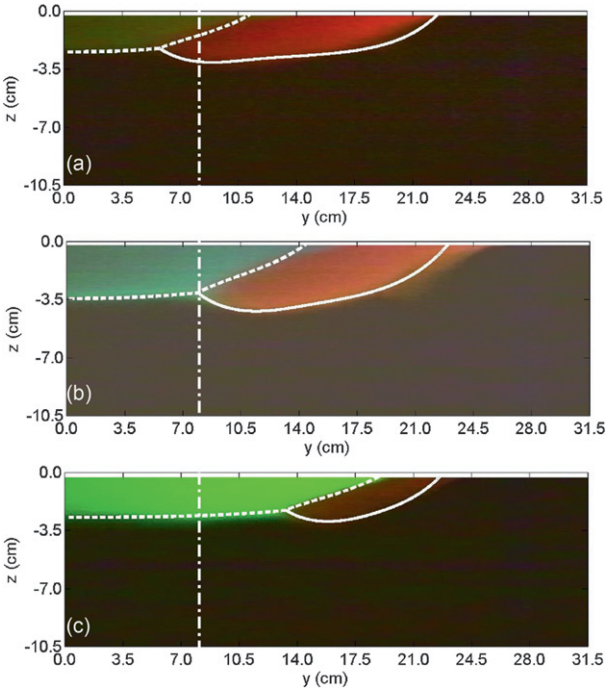

FIG. 9. Side view of the two buoyant currents after reaching the geostrophic equilibrium for $\Gamma_1 = 1.2$ and $\Gamma_2 = 0.7$: (a) $B_1 = 0.63$ and $B_2 = 0.21$; (b) $B_1 = 0.56$ and $B_2 = 0.31$; and (c) $B_1 = 0.32$ and $B_2 = 0.52$. The lines in the figure have the same meaning as in Fig. 8. The dashed–dotted line indicates the position of $y = l_1$ in (b).

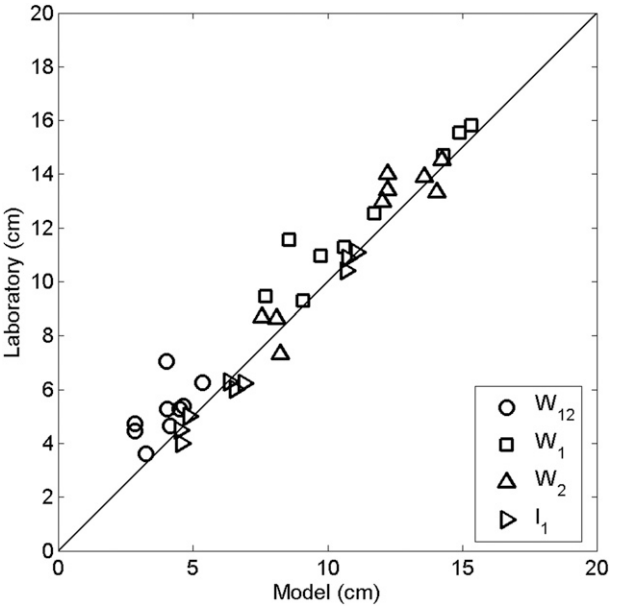

FIG. 10. Comparison of the model prediction of the variables W_{12}, W_1, W_2, and l_1 with the values measured in the laboratory from images like those presented in Figs. 8 and 9. Here, l_1 presents the smallest rms error ($e_{\text{rms}} = 0.37$ cm) between the laboratory measurements and the model predictions, while W_2, W_1, and W_{12} have rms errors of 0.98, 1.31, and 1.47 cm, respectively. Much of the rms error can be accounted for by the presence of a surface Ekman layer in the laboratory, which causes the model prediction of W_1, W_2, and W_{12} to be biased low relative to the laboratory measurements.

identified and used as the reference point to compare the model to the laboratory results. The parabolic deflection of the free surface due to the rotation of the system observed in the laboratory experiments is small and it is ignored in the model formulation. The free surface height difference between the center of rotation ($y = 0$ cm) and a radius of approximately 22 cm is 0.06 cm.

The model does an excellent job in predicting the depth of the two buoyant fluids after they reach a geostrophic equilibrium. In particular, the laboratory experiments confirm that for values of Γ_1, and Γ_2 on the order of unity the alignment is mainly vertical (Fig. 8a), while for larger values of these two nondimensional parameters the alignment becomes horizontal (Fig. 8c). The width of the front between fluids 1 and 2, W_{12}, decreases for increasing values of Γ_1 and Γ_2, while the location of $y = l_1$ is similar since the three experiments in Fig. 8 have comparable values of B_1. The offshore extent of the outer front is similar for these experiments given the similarity in B_2.

For values of Γ_1, and Γ_2 on the order of unity, an increasing value of the lightest fluid Burger number B_1 moves the inner front closer to the coastline (Fig. 9), while an increasing value of B_2 produces a decrease of W_2. Hence, an increasing value of B_1 together with a decreasing value of B_2 moves the inner front closer to the coastline while leaving the offshore position of the outer front mainly unmodified (Figs. 9a,b), while a decreasing value of B_1 together with an increasing value of B_2 moves the inner front offshore while leaving the offshore position of the outer front mainly unmodified (Figs. 9b,c). Note how the width of the front between fluids 1 and 2, W_{12}, remains approximately constant in Fig. 9, while W_1 and W_2 change due to the change in Burger number of the two buoyant fluids.

The magnitude of the variables W_{12}, W_1, W_2, and l_1 is measured for each laboratory experiment using images like those presented in Figs. 8 and 9. The model prediction of these variables is in very good agreement with the laboratory measurements, as shown in Fig. 10. The root-mean-square (rms) error between the laboratory measurements and the model prediction is defined as

$$e_{\text{rms}} = \sqrt{\frac{\sum_{i}^{M} (F_e^i - F_m^i)^2}{M}}, \tag{10}$$

where M is the number of experiments, F is the variable of interest, and a superscript i denotes the ith experiment. As indicated in Fig. 10, l_1 has the smallest rms

error (e_{rms} = 0.37 cm) between the laboratory measurements and the model predictions, while W_2, W_1, and W_{12} have rms errors of 0.98, 1.31, and 1.47 cm, respectively. The small differences observed between the model prediction and the laboratory experiments are thought to be due primarily to two factors: mixing and viscosity. The density differences between the three fluids are obtained by the presence of different amounts of salt. Hence, the three fluids are miscible and mixing between them can occur. Care was taken during the experiments to minimize the amount of mixing. However, a very small amount of mixing occurs as visible for example in Fig. 8a between fluid 2 (red) and fluid 3 (black) at approximately y = 22 cm. The model considers the two fluids immiscible and cannot capture the continuous variations of density at the interface caused by mixing. Note that mixing will cause the concentration of the fluorescent dye to diminish and therefore the intensity of the dye in the mixing region will be lower, as in Fig. 8a. Furthermore, viscosity will allow the fluid in the laboratory to develop Ekman layers on the free surface and at the interface between different fluids. Viscous dissipation in Ekman layers deforms the depth profile just below the free surface. The model formulation does not include viscosity and the small depth deformation due to the Ekman layers is absent near the free surface. This effect is barely visible in Figs. 8 and 9 since the Ekman layer thickness is on the order of millimeters. However, the substantial difference in the rms error between the variable l_1 and the other variables shown in Fig. 10 can be explained by the presence of Ekman layers in the laboratory. The position of fluid 2 subsurface front marked by l_1 is not affected by the Ekman layer present just below the free surface, and the agreement between the model prediction and the laboratory experiments is very good. The location of the surface fronts (i.e., W_1 and W_2) presents a larger error because the Ekman layer in the laboratory deforms the front near the free surface. In particular, the presence of the surface Ekman layer causes the model prediction of W_1 and W_2 to be biased low relative to the laboratory measurements. This bias probably accounts for much of the rms error.

Finally, the model is formulated in a Cartesian coordinate system while the laboratory experiments present a polar coordinate geometry. This difference will influence the conservation of mass equations (boundary conditions 10 and 11) and the final depth profile. However, for the small Burger numbers considered in the laboratory (i.e., $B_1 \leq 0.6$ and $B_2 \leq 0.8$), the differences in depth profile due to the two coordinate systems are negligible.

The movement of the inner front toward the coastline with increasing B_1 suggested by Fig. 9 is confirmed by all experiments and is in agreement with the model prediction shown in Fig. 5a. The model prediction of l_1 (solid line in Fig. 5a) is obtained with fixed values of Γ_1, Γ_2, and B_2, while the laboratory experiments present different values of the above nondimensional parameters. However, the dependence of l_1 on these nondimensional parameters is very weak, allowing this comparison to be made. The small scatter of the laboratory experiments around the model prediction is mainly due to the difference in depth (i.e., $H_1 = H_2 \neq 2.5$ cm) for some of the laboratory experiments (Table 1). The values of W_2 and W_{12} are strongly dependent on the values of Γ_1, Γ_2, and B_2 (see Fig. 5b) and a comparison between the laboratory measurements and the model predictions presented in Fig. 5a cannot be attempted. The decrease in magnitude of W_2 with increasing B_2 shown in Fig. 9 is also supported by the other laboratory experiments. The variation of W_2 with B_2 in the laboratory is compared with the model prediction in Fig. 5b. The model prediction of W_2 is obtained with fixed values of B_1, but the dependence is weak. However, the dependence of W_2 on Γ_1 and on Γ_2 is very strong, as indicated by the three different thick lines in Fig. 5b (the dependence on $H_1 = H_2$ is similarly strong; not shown). The laboratory data present a larger scatter compared to that in Fig. 5a. This is due to the fact that the measurements of W_2 have a larger error than l_1 because of the presence of Ekman layers and because some of the experiments have different initial depths than used in the model ($H_1 = H_2 \neq 2.5$ cm; Table 1).

6. Conclusions

The geostrophic adjustment of two buoyant fluids of different densities in a third denser ambient fluid is presented using both an analytical model and laboratory experiments. In the laboratory, the two buoyant fluids initially at rest evolve to generate two buoyant currents whose vertical and horizontal alignment is controlled primarily by two nondimensional parameters, Γ_1 and Γ_2. Furthermore, the Burger number of the two buoyant fluids controls the location of the fronts relative to the coastline.

The prediction of the model of a geostrophic adjustment of two buoyant fluids compares favorably with the laboratory experiments, enabling us to extend the range of values of the nondimensional numbers achievable in the laboratory and come to the following conclusions. After reaching the geostrophic equilibrium, the two buoyant coastal currents align mainly horizontally for $\Gamma_1 \gg 1$ and $\Gamma_2 \gg 1$ with very little vertical overlap (Figs. 2b, 8c). In the case in which $\Gamma_1 \approx \Gamma_2 \approx 1$, the buoyant currents align mainly vertically (Figs. 2a, 8a). Furthermore, an increasing value of B_1 moves the position of the inner front toward the coastal wall, while an increasing value of B_2 moves the position of the outer front toward the coastline (Figs. 4, 5, 9).

The laboratory results suggest that the solutions found with the analytical model are unstable. However, we believe that the results found in this study are applicable to unstable buoyant coastal currents. Although the frontal instability changes the frontal location in time, the solutions found with the model should apply to unstable coastal currents when the variables of interest are suitably integrated in time for a period that is much longer than the evolution of a singular wave perturbation. For example, although an instantaneous observation of two adjacent buoyant coastal current that are unstable may look different than the model prediction, a time average location of the two fronts should still agree with the model prediction and the alignment of the two fronts should still depend on the nondimensional numbers discussed above. In the present study, the experimental set up used to generate buoyant currents relies on a constant volume of buoyant fluid (section 4). To test the above prediction the current needs to have a constant supply of buoyant fluid, as occurs in nature, in order to replenish the buoyant fluid lost to the ambient via the eddies generated by the instability. Future contributions will focus on the stability of the two buoyant fronts and the applicability of the model results to unstable buoyant currents.

The present study, albeit very idealized, brings some insights on how the water masses of two individual buoyant coastal currents align relative to each other vertically and horizontally. For example, in the scenario in which fluid 2 is polluted or contains harmful algae, one could be concerned with the likelihood of fluid 2 reaching the coastline. In the absence of downwelling-favorable winds, the results of the present study suggest the following. For $B_1 \ll 1$, the water mass of fluid 2 should flow far away from the coastline, which may ensure that the pollution or harmful algae remain offshore. For values of B_1 and B_2 $O(1)$, $\Gamma_1 \gg 1$, and $\Gamma_2 \gg 1$, the alignment of the two buoyant currents should be mainly horizontal; hence, vertical mixing generated by winds or tides should occur primarily between the polluted waters (fluid 2) and the open ocean (fluid 3). Only a small part of the current close to the coastline (fluid 1) should mix with the polluted current (fluid 2), and the mixed polluted waters should remain offshore. The pollutants or harmful algae should be expected to arrive closer to the coastline for $B_1 \gg 1$, when the interfacial front between fluids 1 and 2 is close to the coastline, and for B_1 and B_2 being $O(1)$ and $\Gamma_1 \approx \Gamma_2 \approx 1$. In the latter case, the alignment of the two buoyant currents should be mainly vertical. Hence, mixing generated by winds or tides should occur primarily between the polluted waters (fluid 2) and the fluid close to the coastline (fluid 1), increasing the likelihood of the polluted waters reaching the coastline. The above interpretation of the present results of a very idealized model and laboratory experiments is highly speculative and should be interpreted with care. However, it highlights how idealized studies such as the present one may bring insight in interpreting more complex models and oceanic observations. Our model and laboratory experiments do not take into account two important forcings present in the ocean: winds and tides.

Winds are intermittent events and our results should apply when winds are absent or low. Upwelling and downwelling winds have been shown to significantly change the structure of buoyant plumes (e.g., Fong et al. 1997; Fong and Geyer 2001; Garcia Berdeal et al. 2002; Lentz 2004; Geyer et al. 2004; Hetland and Signell 2005). Upwelling winds, for example, tend to spread the plume oceanward, cause it to thin, and thereby enhance vertical mixing with the ambient ocean water. Downwelling winds tend to push the plume toward the coast and thicken it and will clearly modify the likelihood of offshore pollutants reaching the coastline. Upwelling-favorable winds enhance vertical mixing processes, but the relative alignment of the two buoyant currents should be maintained since the system as a whole is moved offshore.

Tides will increase vertical mixing, via bottom boundary generated turbulence, which may influence the buoyant currents in shallow waters near the coast, particularly within the estuary and the near-field region of the entrance of the plume into the coastal ocean (MacDonald et al. 2007). The effects of tides will be to change the initial conditions of our model or laboratory experiments but should not dramatically influence the alignment of buoyant currents along the coast, downstream of estuary sources, where tidal currents are comparatively weak.

Further work is necessary to determine the relevance of this idealized study to real buoyant coastal currents composed by waters emanating from different sources under realistic forcing by tides and winds.

Acknowledgments. CC wishes to thank Jason Hyatt for carefully reading drafts and substantially improving the clarity of the manuscript. We thank Joe Pedlosky and Karl Helfrich for helpful comments and invaluable discussions. The laboratory experiments were carried out with the able assistance of Anders Jensen. Support was given by the National Science Foundation Project OCE-0726339 and by the Marie Curie Fellowship from the Seventh Framework Programme (FP7) of the European Commission.

REFERENCES

Artegiani, A., D. Bregant, E. Paschini, N. Pinardi, F. Raicich, and A. Russo, 1997: The Adriatic Sea general circulation. Part II: Baroclinic circulation structure. *J. Phys. Oceanogr.,* **27,** 1515–1532.

Cenedese, C., and P. F. Linden, 2002: The stability of a buoyancy driven coastal current at the shelfbreak. *J. Fluid Mech.,* **452,** 97–121.

Chabert d'Hieres, G., H. Didelle, and D. Obaton, 1991: A laboratory study of surface boundary currents: Application to the Algerian Current. *J. Geophys. Res.,* **96,** 12 539–12 548.

Chapman, D. C., and S. J. Lentz, 1994: Trapping of a coastal density front by the bottom boundary layer. *J. Phys. Oceanogr.,* **24,** 1464–1479.

Churchill, J. H., N. R. Pettigrew, and R. P. Signell, 2005: Structure and variability of the western Maine coastal current. *Deep-Sea Res. II,* **52,** 2392–2410.

Csanady, G. T., 1971: On the equilibrium shape of the thermocline in a shore zone. *J. Phys. Oceanogr.,* **1,** 263–270.

——, 1979: The birth and death of a warm core ring. *J. Geophys. Res.,* **84,** 777–780.

Fong, D. A., and W. R. Geyer, 2001: Response of a river plume during an upwelling favorable wind event. *J. Geophys. Res.,* **106,** 1067–1084.

——, and ——, 2002: The alongshore transport of freshwater in a surface-trapped river plume. *J. Phys. Oceanogr.,* **32,** 957–972.

——, ——, and R. P. Signell, 1997: The wind-forced response on a buoyant coastal current: Observations of the western Gulf of Maine plume. *J. Mar. Syst.,* **12,** 69–81.

Franks, P. J. S., and D. M. Anderson, 1992: Alongshore transport of a toxic phytoplankton bloom in a buoyancy current: Alexandrium tamarense in the Gulf of Maine. *Mar. Biol.,* **112,** 153–164.

Garcia Berdeal, I., B. M. Hickey, and M. Kawase, 2002: Influence of wind stress and ambient flow on a high discharge river plume. *J. Geophys. Res.,* **107,** 3130, doi:10.1029/2001JC000932.

Garvine, R. W., 1999: Penetration of buoyant coastal discharge onto the continental shelf: A numerical model experiment. *J. Phys. Oceanogr.,* **29,** 1892–1909.

——, 2001: The impact of model configuration in studies of buoyant coastal discharge. *J. Mar. Res.,* **59,** 193–225.

Geyer, W. R., R. P. Signell, D. A. Fong, J. Wang, D. M. Anderson, and B. A. Keafer, 2004: The freshwater transport and dynamics of the Western Maine Coastal Current. *Cont. Shelf Res.,* **24,** 1339–1357.

Gill, A. E., 1982: *Atmosphere–Ocean Dynamics.* Academic Press, 662 pp.

Griffiths, R. W., and P. F. Linden, 1981a: The stability of buoyancy-driven coastal currents. *Dyn. Atmos. Oceans,* **5,** 281–306.

——, and ——, 1981b: The stability of vortices in rotating, stratified fluid. *J. Fluid Mech.,* **105,** 283–316.

——, and ——, 1982: Laboratory experiments on fronts. Part I: Density-driven boundary currents. *Geophys. Astrophys. Fluid Dyn.,* **19,** 159–187.

——, and E. J. Hopfinger, 1983: Gravity currents moving along a lateral boundary in a rotating frame. *J. Fluid Mech.,* **134,** 357–399.

Hetland, R. D., 2005: Relating river plume structure to vertical mixing. *J. Phys. Oceanogr.,* **35,** 1667–1688.

——, and R. P. Signell, 2005: Modelling coastal current transport in the Gulf of Maine. *Deep-Sea Res. II,* **52,** 2430–2449.

Horner-Devine, A. R., D. A. Fong, S. G. Monismith, and T. Maxworthy, 2006: Laboratory experiments simulating a coastal river discharge. *J. Fluid Mech.,* **555,** 203–232.

Hsueh, Y., and B. Cushman-Roisin, 1983: On the formation of surface to bottom fronts over steep topography. *J. Geophys. Res.,* **88,** 743–750.

Lentz, S., 2004: The response of buoyant coastal plumes to upwelling-favorable winds. *J. Phys. Oceanogr.,* **34,** 2458–2469.

——, and K. R. Helfrich, 2002: Buoyant gravity currents along a sloping bottom in a rotating fluid. *J. Fluid Mech.,* **464,** 251–278.

MacDonald, D. G., L. Goodman, and R. D. Hetland, 2007: Turbulent dissipation in a near field river plume: A comparison of control volume and microstructure observations with a numerical model. *J. Geophys. Res.,* **112,** C07026, doi:10.1029/2006JC004075.

Nof, D., 2005: The momentum imbalance paradox revisited. *J. Phys. Oceanogr.,* **25,** 1928–1939.

O'Donnell, J., 1990: The formation and fate of a river plume: A numerical model. *J. Phys. Oceanogr.,* **20,** 551–569.

Ou, H. W., 1983: Some two-layer models of the shelf-slope front: Geostrophic adjustment and its maintenance. *J. Phys. Oceanogr.,* **13,** 1798–1808.

——, 1984: Geostrophic adjustment: A mechanism for frontogenesis. *J. Phys. Oceanogr.,* **14,** 994–1000.

Raicich, F., 1996: On the fresh water balance of the Adriatic Sea. *J. Mar. Syst.,* **9,** 305–319.

Rossby, C. G., 1938: On the mutual adjustment of pressure and velocity distribution in certain simple current systems, II. *J. Mar. Res.,* **2D,** 239–263.

Royer, T. C., 1982: Coastal fresh water discharge in the northeast Pacific. *J. Geophys. Res.,* **87,** 2017–2021.

——, 1998: Coastal processes in the northern North Pacific. *The Sea,* K. H. Brink and A. R. Robinson, Eds., Vol. 11, *Regional Studies and Syntheses,* Wiley and Sons, 395–414.

Simpson, J. E., 1997: The anatomy of a gravity current. *Gravity Currents in the Environment and the Laboratory,* 2nd ed. Cambridge University Press, 140–163.

Stabeno, P. J., N. A. Bond, A. J. Hermann, N. B. Kachel, C. W. Mordy, and J. E. Overland, 2004: Meteorology and oceanography of the northern Gulf of Alaska. *Cont. Shelf Res.,* **24,** 859–897.

van Heijst, G. J. F., 1985: A geostrophic adjustment model of a tidal mixing front. *J. Phys. Oceanogr.,* **15,** 1182–1190.

Yankovsky, A. E., and D. C. Chapman, 1997: A simple theory for the fate of buoyant coastal discharges. *J. Phys. Oceanogr.,* **27,** 1386–1401.